7-1-1999

Observations and Interpretation of Gravity Wave Induced Fluctuations in the O I (557.7 nm) Airglow

G. Schubert
Institute of Geophysics and Planetary Physics, University of California

R. L. Walterscheid
The Aerospace Corporation

Michael P. Hickey Ph.D.
Embry-Riddle Aeronautical University, hicke0b5@erau.edu

C. A. Tepley
Arecibo Observatory, Arecibo, Puerto Rico

JOURNAL OF GEOPHYSICAL RESEARCH, VOL. 104, NO. A7, PAGES 14,915–14,924, JULY 1, 1999

Observations and interpretation of gravity wave induced fluctuations in the O I (557.7 nm) airglow

G. Schubert and R. L. Walterscheid
Space Sciences Laboratory, The Aerospace Corporation, Los Angeles, California

M. P. Hickey
Department of Physics and Astronomy, Clemson University, Clemson, South Carolina

C. A. Tepley
Arecibo Observatory, Arecibo, Puerto Rico

Abstract. Observations of fluctuations in the intensity and temperature of the O I (557.7 nm) airglow taken at Arecibo in 1989 are reported and interpreted on the assumption that they are caused by gravity waves propagating through the emission layer. The data give the magnitude of Krassovsky's ratio as 3.5 ± 2.2, at periods between about 5 and 10 hours. Comparison with theory shows that the gravity waves responsible for the measured airglow variations must have long wavelengths of several thousand kilometers. The observed phases of Krassovsky's ratio are in good agreement with theoretically predicted values at the long wavelengths and large periods for about half the cases. In the other cases, observed phases are near $-180°$, suggesting that the waves responsible for the airglow fluctuations have experienced strong reflections in the emission layer. The observations emphasize the importance of knowing the full altitude profiles of temperature and winds for extraction of wave information from the airglow fluctuations.

1. Introduction

Rocket, ground-based, and satellite observations of the O I (557.7 nm) or O(^1S) airglow have been a primary source of information about the structure and dynamics of the upper mesosphere at altitudes around 97 km, where the emission rate of the atomic oxygen green line is a maximum. The literature on the O I (557.7 nm) airglow has mostly focused on elucidating the relevant photochemistry and deducing the altitude profile of atomic oxygen number density from height variations of the emission rate [e.g., *Chapman*, 1931; *Barth*, 1961, 1964; *Slanger and Black*, 1977; *Witt et al.*, 1979; *Thomas et al.*, 1979; *Thomas*, 1981; *Bates*, 1981, 1988, 1992; *Torr et al.*, 1985; *McDade et al.*, 1986; *McDade and Llewellyn*, 1986; *Greer*, 1988; *Murtagh et al.*, 1990; *Sharp*, 1991; *Kita et al.*, 1992; *Gobbi et al.*, 1992; *Lopez-Gonzalez et al.*, 1992a, b; *Melo et al.*, 1997].

New instrumentation and multiinstrument campaigns have recently made possible the study of gravity waves and tides using observations of the O I (557.7 nm) airglow. *Hickey et al.* [1997] used O(^1S) nightglow intensity fluctuations and wave parameters observed by a two-dimensional (2-D) all-sky CCD imaging system over Arecibo in January 1993 [*Taylor and Garcia*, 1995] to simulate the propagation of two gravity waves through the mesopause region. In a similar study, *Hickey et al.* [1998] modeled small-scale mesospheric gravity waves observed in the O I (557.7 nm) nightglow during the Airborne Lidar Observations of Hawaiian Airglow (ALOHA) 1993 campaign. *Makhlouf et al.* [1997] have also used data on O I (557.7 nm) brightness fluctuations and gravity wave parameters from a ground-based CCD all-sky imager to infer a value for the vertical eddy diffusion coefficient due to gravity waves in the 90–100 km altitude interval.

The above efforts notwithstanding, O(^1S) observations remain a largely untapped resource of information about gravity waves in the mesosphere. In this paper we investigate how measurements of fluctuations in the O I (557.7 nm) airglow can be used to quantitatively infer the characteristics of the gravity waves driving the fluctuations. Our approach is similar to that of previous studies of gravity wave driven fluctuations in the OH [*Walterscheid et al.*, 1987; *Schubert and Walterscheid*, 1988; *Schubert et al.*, 1991; *Hickey et al.*, 1992; *Makhlouf et al.*, 1995] and O_2 atmospheric (0–1) [*Hickey et al.*, 1993a] airglow which make use of Krassovsky's [1972] ratio to relate the fluctuations in airglow intensity to the fluctuations in temperature of the emitting gas. We summarize the theory needed to apply Krassovsky's ratio to the O I (557.7 nm) airglow fluctuations and use this theory to interpret measurements of the airglow temperature and intensity fluctuations.

The measurements of the O(^1S) airglow were made at the Arecibo Observatory in Puerto Rico during the Arecibo Initiative for Dynamics of the Atmosphere (AIDA) 1989 campaign. We used a single-etalon Fabry-Perot interferometer to obtain information on the integrated area, width, and relative Doppler shift of this emission line, for which we derived the intensity, temperature, and background winds of the lower thermosphere. Intensity and temperature fluctuations were extracted from the time variation of the measurements to compare with the theory.

2. Theory

Theories that describe how fluctuations in the intensity of the O(^1S) airglow are produced by gravity wave disturbances

Paper number 1999JA900096.
0148-0227/99/1999JA900096$09.00

Table 1. Chemistry of the $O(^1S)$ Nightglow Model

Reaction	Rate of Reaction*
$O + O + M \rightarrow O_2 + M$	$k_1 = 4.7 \times 10^{-33} (300/T)^2$
$O + O + M \rightarrow O_2(c^1\Sigma_u^-) + M$	$k = \zeta k_1$, $\zeta = 0.03$
$O_2(c^1\Sigma_u^-) + O_2 \rightarrow O_2(b^1\Sigma_g^+) + O_2$	$k_2 = 5.0 \times 10^{-13}$
$O_2(c^1\Sigma_u^-) + O \rightarrow O_2 + O$	$k_3 = 3.0 \times 10^{-11}$
$O_2(c^1\Sigma_u^-) + O \rightarrow O_2 + O(^1S)$	$k = \delta k_3$, $\delta = 0.2$
$O_2(c^1\Sigma_u^-) \rightarrow O_2 + h\nu$	$A_1 = 2.0 \times 10^{-2}$
$O(^1S) + O_2 \rightarrow O(^3P) + O_2$	$k_6 = 4.0 \times 10^{-12} \exp(-865/T)$
$O(^1S) \rightarrow O + h\nu$ (5577 Å, 2972 Å)	$A_2 = 1.105$
$O(^1S) \rightarrow O + h\nu$ (5577 Å)	$A_{5577} = 1.06$

*Units are s^{-1}, $cm^{-3}\ s^{-1}$, and $cm^{-6}\ s^{-1}$ for unimolecular, bimolecular, and termolecular reactions, respectively.

have been presented by *Hickey et al.* [1993a, b, 1997, 1998] and *Makhlouf et al.* [1997, 1998]. Here we follow and further develop the approach of *Hickey et al.* [1997, 1998]. Here we follow and further develop the approach of *Hickey et al.* [1997].

The ground-based spectrophotometric observations provide data on the vertically integrated airglow intensity $\langle I \rangle = \langle \bar{I} \rangle + \langle I' \rangle$ (I is intensity, angle brackets denote integration over the height of the emission region, the overbar refers to a time-averaged background state, and the prime denotes departures therefrom) and the intensity-weighted temperature $\langle T_I \rangle = \langle \bar{T}_I \rangle + \langle T_I' \rangle$ ($\langle T_I \rangle = \int dz TI / \langle I \rangle$ (z is the vertical coordinate). The transfer function $\langle \eta \rangle$ between the gravity wave driven fluctuations in intensity-weighted temperature and the fluctuations in vertically integrated intensity is Krassovsky's ratio [*Krassovsky*, 1972; *Schubert et al.*, 1991]

$$\langle \eta \rangle = \frac{\langle I' \rangle / \langle \bar{I} \rangle}{\langle T_I' \rangle / \langle \bar{T}_I \rangle} \tag{1}$$

Airglow observations provide values for the amplitude and phase of the complex Krassovsky's ratio according to (1). Values of $\langle \eta \rangle$ from dynamical-chemical theory can be compared with the observational values of $\langle \eta \rangle$ to infer information about the airglow chemistry, the gravity wave field, the winds, and the atmospheric structure, as has been done in the above cited studies of the OH airglow.

The intensity of the atomic oxygen green line nightglow is directly proportional to the number density of the emitting species $n[O(^1S)] = \bar{n}[O(^1S)] + n'[O(^1S)]$. Therefore we can write the numerator of (1) as

$$\frac{\langle I' \rangle}{\langle \bar{I} \rangle} = \frac{\langle n'[O(^1S)] \rangle}{\langle \bar{n}[O(^1S)] \rangle} \tag{2}$$

The determination of the fluctuation in the number density of $O(^1S)$ uses the linearized continuity equation

$$i\omega n' = P' - L' - w' \frac{\partial \bar{n}}{\partial z} - \bar{n} \nabla \cdot \mathbf{v}' \tag{3}$$

where P' and L' are the perturbations in the chemical production and loss of $O(^1S)$, respectively; n' is the $O(^1S)$ number density perturbation about its mean value $\bar{n}$; w' is the gravity wave vertical velocity component; $\nabla \cdot \mathbf{v}'$ is the gravity wave velocity divergence; and ω is the angular frequency of the gravity wave. All perturbation quantities are assumed to vary as $\exp i(\omega t - kx)$, where k is the horizontal wavenumber in the x direction. Specification of the chemical production and loss terms in (3) requires identification of the chemical reactions involved in the $O(^1S)$ chemistry. These reactions involve other minor species whose number densities must also be determined. Fluctuations in the number densities of all minor species are determined from continuity equations identical to (3).

The $O(^1S)$ chemistry is given in Table 1. We have assumed, in accordance with *Bates* [1988], that the production of $O(^1S)$ is by the two-step Barth process in which the intermediate state is $O_2(c^1\Sigma_u^-)$. The reaction rates employed here are those given by *Torr et al.* [1985], except for the branching ratios related to the production of $O_2(c^1\Sigma_u^-)$ and $O(^1S)$, which are taken from *Lopez-Gonzalez et al.* [1992a, b]. The Barth process chemistry couples the species O, $O_2(c^1\Sigma_u^-)$, and $O(^1S)$, and the fluctuations in the number densities of these constituents must be determined by the simultaneous solution of (3) for each of these species. The specific form of these equations is given in (A3)–(A5) of *Hickey et al.* [1997].

The solution of the linearized continuity equations for the minor species O, $O_2(c^1\Sigma_u^-)$, and $O(^1S)$ depends on the complex dynamical factors f_1, f_2, and f_3 that relate the velocity divergence $\nabla \cdot \mathbf{v}'$, the vertical velocity perturbation w', and the major gas density perturbation $n'(M)$ to the temperature perturbation T'

$$\nabla \cdot \mathbf{v}' = f_1 \frac{T'}{\bar{T}} \tag{4}$$

$$w' = f_2 \frac{T'}{\bar{T}} \tag{5}$$

$$\frac{n'(M)}{\bar{n}(M)} = f_3 \frac{T'}{\bar{T}} \tag{6}$$

A model for the upward propagation of gravity waves is needed to determine the dynamical factors f_1, f_2, and f_3 and the altitude variation of $T'/\bar{T}$. We use the full wave, gravity wave model of *Hickey et al.* [1994, 1995, 1997, 1998] for the propagation of nonhydrostatic, linear gravity waves from the troposphere up to a maximum altitude of 500 km. It includes dissipation due to eddy processes in the lower atmosphere and molecular processes (viscosity, thermal conduction, and ion drag) in the upper atmosphere, height variations of the mean temperature and horizontal winds, and Coriolis forces. The model accurately describes the propagation of gravity waves in an inhomogeneous atmosphere.

3. Inputs and Derived Quantities for the Basic State

Mean state quantities required for the full wave computations are provided by the mass spectrometer/incoherent scatter (MSIS-90) model [*Hedin*, 1991]. The altitude profile of mean state temperature is shown in Figure 1. The mesopause is at an altitude of 98 km where the temperature is 181.4 K. Mean state major gas number density $\bar{n}(M)$ versus altitude is shown in Figure 2. Major gas number density decreases nearly exponentially with height in the altitude interval 75–110 km with an approximate scale height H of 6 km. Momentum and thermal diffusivities are plotted as a function of altitude in Figure 3. The molecular coefficients of viscosity μ_m and thermal conductivity k_m are taken from *Rees* [1989] and are used to calculate the molecular momentum diffusivity $\eta_m = \mu_m/\rho$ and molecular thermal diffusivity $k_m/\rho c_p$. The eddy momentum diffusivity η_e approximates that given by *Strobel* [1989]. The eddy thermal diffusivity κ_e is calculated from the eddy momen-

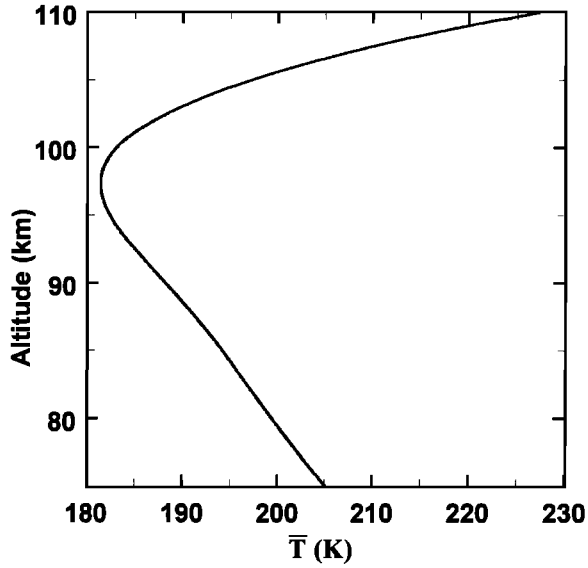

Figure 1. Altitude profile of mean state temperature from the MSIS-90 model [*Hedin*, 1991].

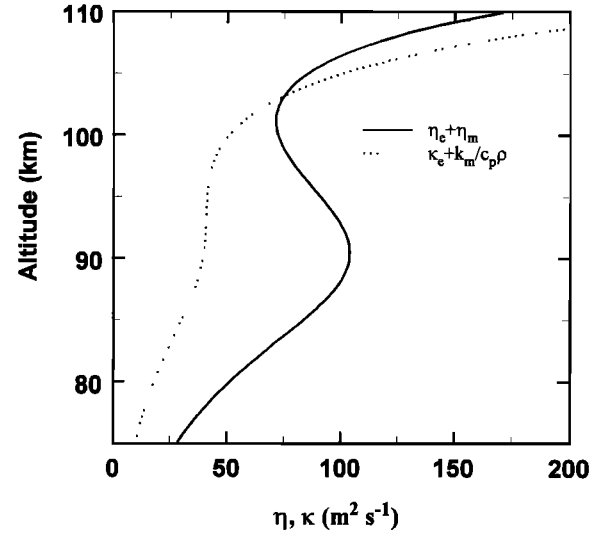

Figure 3. Height profiles of momentum η and thermal κ diffusivities.

tum diffusivity by assuming a Prandtl number of 3 [*Strobel*, 1989]. The increase of both momentum and thermal diffusivity with height between 75 and 90 km altitude is thus due to the dominance, and increase with height, of both eddy diffusivities in this altitude range. The increase of both diffusivities with height above the mesopause is due to the dominance, and increase with height, of the molecular diffusivities.

The solution of the linearized continuity equations for the minor species O, $O_2(c^1\Sigma_u^-)$, and $O(^1S)$ also requires mean state values for $\bar{n}(O)$, $\bar{n}[O_2(c^1\Sigma_u^-)]$, and $\bar{n}(O(^1S))$. We employ the altitude profile of undisturbed atomic oxygen density derived from the MSIS-90 model for April 10 at 18°N for approximately local midnight conditions (Figure 4). At an altitude of 97.9 km, $\bar{n}(O)$ is a maximum and varies little with height in the altitude range 90–100 km. The chemistry of Table 1 allows us to determine $\bar{n}(O_2(c^1\Sigma_u^-))$, and $\bar{n}[O(^1S)]$ as

$$\bar{n}[O_2(c^1\Sigma_u^-)] = \frac{\xi k_1 \bar{n}^2(O)\bar{n}(M)}{k_2\bar{n}(O_2) + k_3\bar{n}(O) + A_1} \tag{7}$$

$$\bar{n}[O(^1S)] = \frac{\delta k_3 \bar{n}(O)\bar{n}[O_2(c^1\Sigma_u^-)]}{k_6\bar{n}(O_2) + A_2} \tag{8}$$

Altitude profiles of the mean state densities of $O_2(c^1\Sigma_u^-)$ and $O(^1S)$ are also shown in Figure 4. The altitude profiles of $\bar{n}[O_2(c^1\Sigma_u^-)]$ and $\bar{n}[O(^1S)]$ are similar; both mean state number densities increase approximately exponentially with height between the altitudes of 75 km and about 95 km with an approximate scale height of −1 km. At heights above their respective maxima, $\bar{n}[O_2(c^1\Sigma_u^-)]$ and $\bar{n}[O(^1S)]$ decrease approximately exponentially with altitude with an approximate scale height of 3 km.

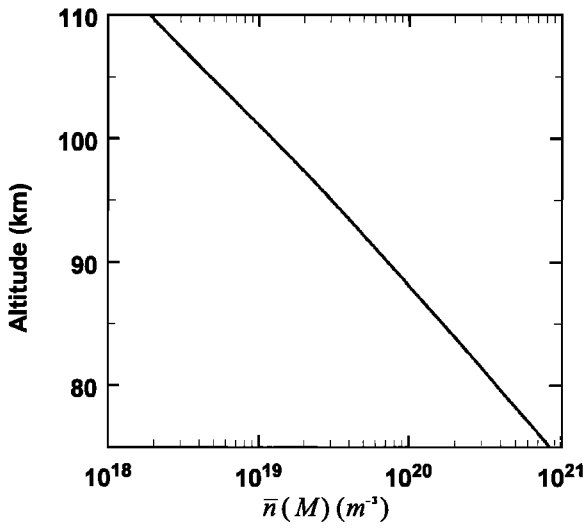

Figure 2. Altitude profile of mean state major gas number density from the MSIS-90 model [*Hedin*, 1991].

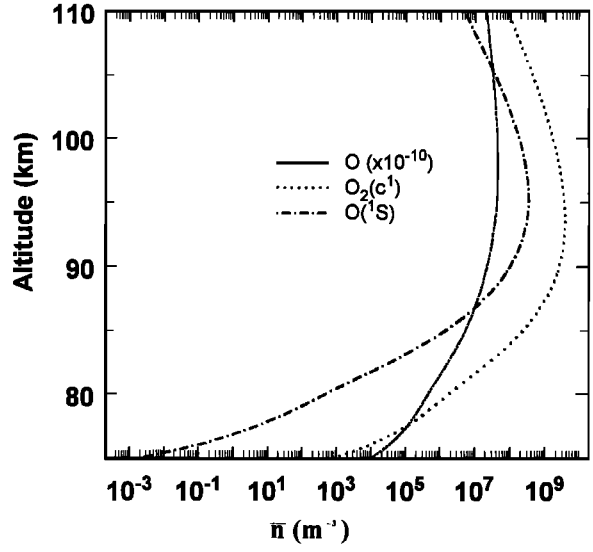

Figure 4. Height profiles of mean state minor species number densities $\bar{n}(O)$, $\bar{n}(O_2[c^1\Sigma_u^-])$, *and* $\bar{n}[O(^1S)]$. $\bar{n}(O)$, is from the MSIS-90 model for April 10 at 18°N [*Hedin*, 1991]. The values of $\bar{n}[O_2[c^1\Sigma_u^-)]$ and $\bar{n}[O(^1S)]$ are from (7) and (8), respectively.

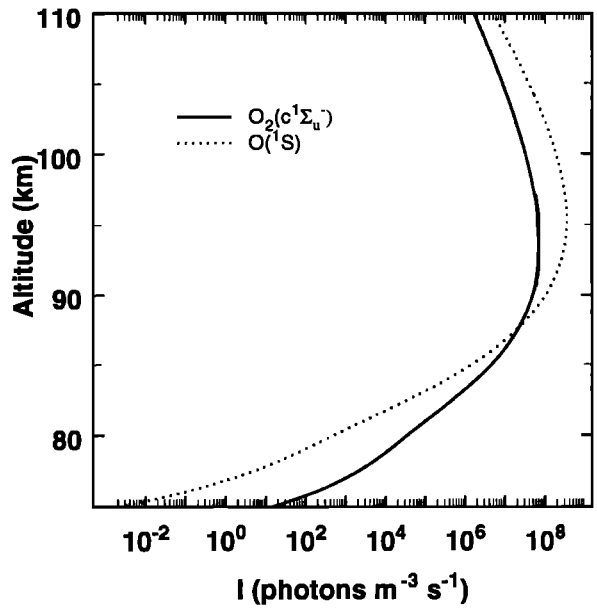

Figure 5. Altitude profiles of the background intensities of the $O(^1S)$ and $O_2(c^1\Sigma_u^-)$ airglows.

The $O(^1S)$ emission intensity resulting from the chemical scheme of Table 1 is shown in Figure 5 $\{\bar{I} \propto A_{5577}\bar{n}[O(^1S)]\}$. The $O(^1S)$ emission layer peaks near 95 km altitude with a full width at half maximum of about 9 km. The $O_2(c^1\Sigma_u^-)$ emission intensity resulting from the chemical scheme of Table 1 is also shown in Figure 5 $\{\bar{I} \propto A_1\bar{n}[O_2(c^1\Sigma_u^-)]\}$. The $O_2(c^1\Sigma_u^-)$ emission layer peaks near 93.6 km altitude with a full width at half maximum of about 10.8 km.

4. Dynamical Factors f_1, f_2, and f_3; A Comparison of Full Wave and WKB Results

As discussed in section 3, the dynamical effects of gravity waves on airglow intensity are controlled by the factors f_1, f_2, and f_3. In this section we discuss how these factors vary with gravity wave period. We also discuss how the dynamical factors, computed using the full wave (FW) theory, differ from the dynamical factors based on the WKB approximation employed in many of our previous papers [e.g., *Schubert et al.*, 1991; *Hickey et al.*, 1993a]. The factors are shown as a function of period in Figure 6 for a horizontal wavelength λ_x of 1000 km evaluated at an altitude of 95 km. Results for both the FW theory and WKB approximation are included. In earlier work, there were gaps in the plotted results where the waves were purely evanescent, i.e., k_z purely imaginary [*Walterscheid et al.*, 1987; *Schubert et al.*, 1988]. The absence of similar gaps in the present plots is due to wave dissipation. With dissipation k_z has a real (propagating) component in the gap regions. We will see later that the airglow observations suggest that we are dealing with waves having λ_x of order 1000 km.

The magnitude of f_1 generally decreases with increasing period from a value near 10^{-1} at a period of 100 s to a value between 10^{-3} and 10^{-4} at a period of 10^5 s. The factor f_1 is almost pure imaginary (it has a phase of $-90°$ except at periods of 10^4 to 10^5 s, when its phase differs by a small amount from $-90°$, and at periods in and near a period interval of wave evanescence, which occurs at periods between 10^2 and 10^3 s). The WKB approximation does a reasonable job of representing the FW f_1 except at evanescent periods wherein the WKB approximation fails to account for the nonmonotonic behavior of f_1. The magnitude of f_1 versus period shows nonmonotonic behavior at periods in and around the evanescent period interval. Peaks and troughs in $|f_1|$ versus period occur at the ends of the evanescent period interval.

At periods in excess of about 3×10^4 s (for $\lambda_x = 1000$ km) or at wave phase speeds smaller than about 50 m s^{-1}, the vertical wavelength of the gravity wave is small enough for severe damping to occur. This is illustrated in Figure 7 which compares the ratio of the wave kinetic energy (KE) at 100 km altitude to that at 85 km altitude as a function of wave period on the basis of the FW description of wave propagation. It is seen that dissipation starts to become important at periods of

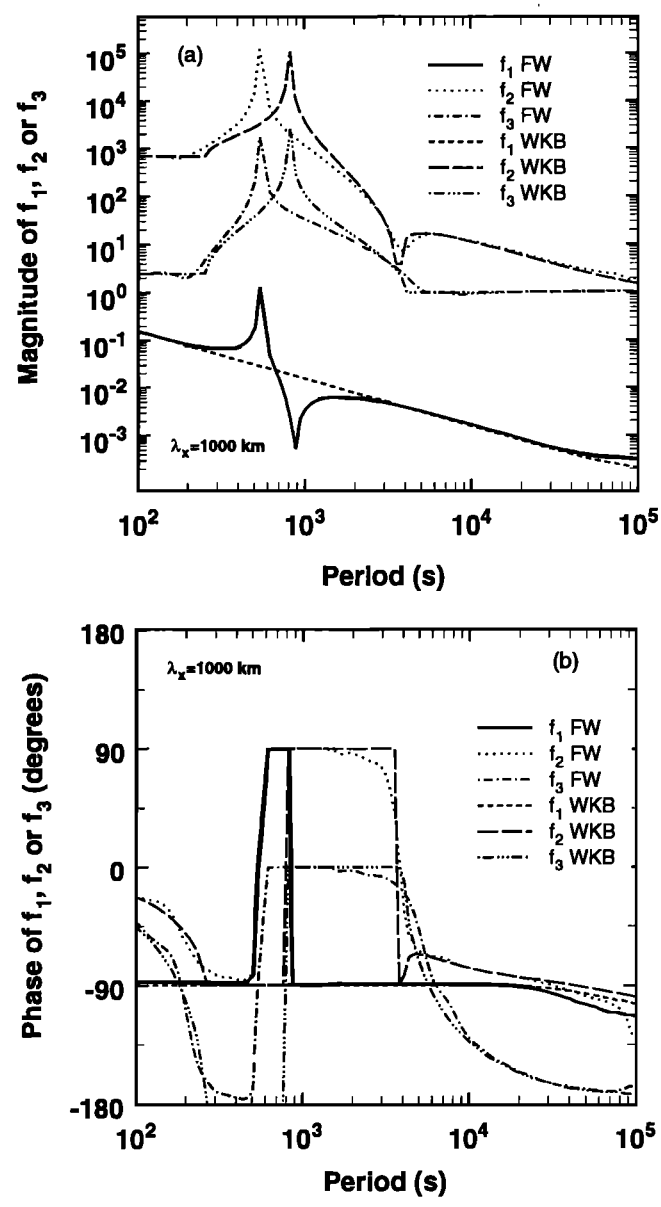

Figure 6. (a) Amplitude and (b) phase of the gravity wave dynamical factors f_1, f_2, and f_3 as a function of period for a horizontal wavelength of 1000 km. Results from a full wave (FW) calculation and from the WKB approximation are shown.

about 2×10^4 s (phase speeds of about 50 m s^{-1}). At a given phase speed, additional calculations show that dissipation is more severe for waves with larger horizontal wavelengths. Waves with phase speeds of about 10 m s^{-1} are highly dissipated with more than 99.999% of the energy lost between 85 and 100 km altitude.

The magnitude of f_2 also generally decreases with increasing period except for more complex behavior associated with the period interval of evanescence; the WKB approximation works rather well in calculating f_2 at most periods, but it fails in and around the evanescent region (Figure 6a). The FW calculation of f_2, as is the case with f_1, is influenced by severe wave damping for periods in excess of about 3×10^4 s. The factor f_3 is essentially of unity magnitude at long gravity wave periods. In the evanescent period interval, f_3 differs substantially from unity. The WKB calculations of f_2 and f_3 do not do well at evanescent periods.

5. Krassovsky's Ratio

Figure 8 shows the amplitude and phase of Krassovsky's ratio $\langle\eta\rangle$ for the O(^1S) airglow as a function of period for a horizontal wavelength of 1000 km. Both FW and WKB results are shown. For periods greater than about 3×10^3 s, the amplitude of $\langle\eta\rangle$ varies from about 4 to 30 and the phase of $\langle\eta\rangle$ varies between about +30° and −60° except near the longest periods plotted where the full wave phase rotates rapidly through large positive values. For the most part, computation of $\langle\eta\rangle$ using the WKB approximation for the waves yields results in approximate agreement with those of the FW calculation. Differences in the magnitude of $\langle\eta\rangle$ between the FW and WKB models are about 20% at a period of 10^4 s (phase speed of 100 m s^{-1}), with the FW results being the larger.

The theory discussed above for determining Krassovsky's ratio for the O(^1S) airglow can also provide $\langle\eta\rangle$ for the O_2 atmospheric airglow. The O_2 atmospheric airglow at 864.5 nm results from the decay of O_2 ($b^1\Sigma_g^+$) (Table 1). A comparison of $\langle\eta\rangle$ versus period at a horizontal wavelength of 1000 km for the O(^1S) and O_2 atmospheric airglows is shown in Figures 9a and b. The Krassovsky ratios for the two airglows are very similar, though there are some quantitative differences in detail. If both airglows are described by the chemistry in Table 1, then observations of both signals provide essentially redundant information about their source region and the driving gravity wave field.

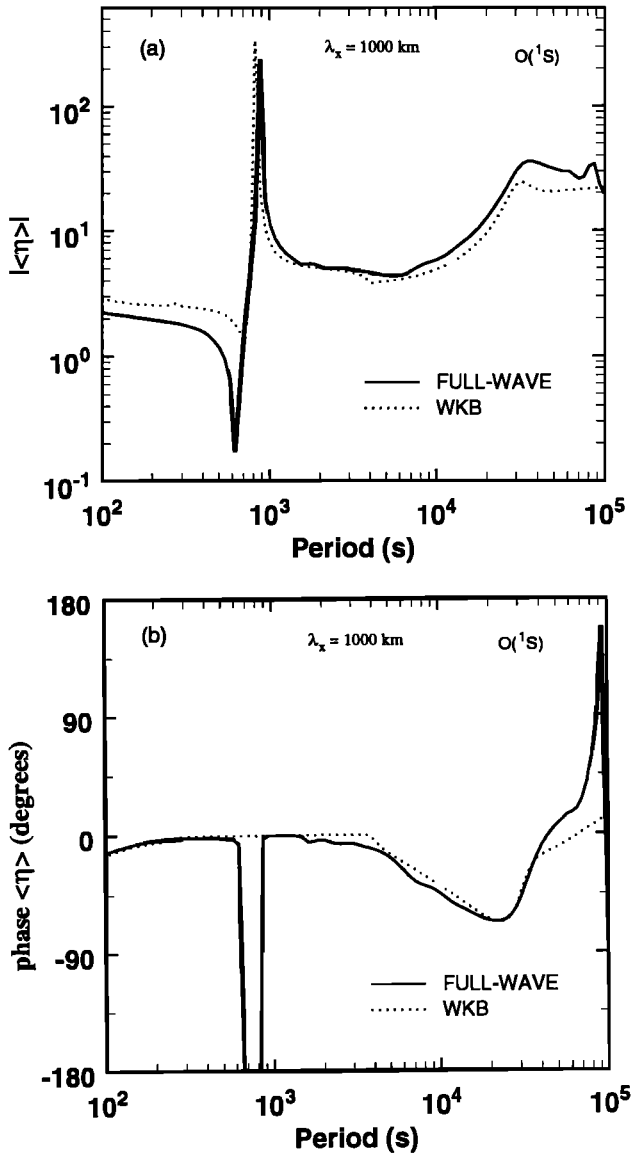

Figure 8. (a) Amplitude and (b) phase of Krassovsky's ratio $\langle\eta\rangle$ versus period for the O(^1S) airglow and a horizontal wavelength λ_x of 1000 km for both the full wave FW theory and the WKB approximation.

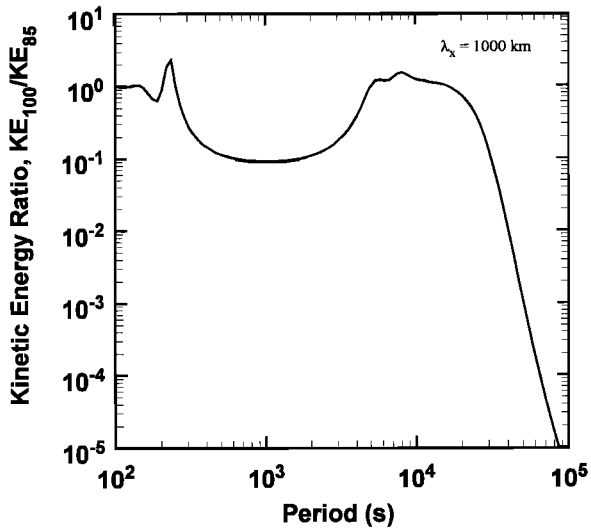

Figure 7. Ratio of wave kinetic energy KE at 100 km altitude to KE at 85 km altitude as a function of period for a horizontal wavelength of 1000 km calculated using the full wave theory.

In sections 6 and 7 we discuss observations of intensity and temperature for the O(^1S) airglow and the values of Krassovsky's ratio inferred therefrom. We then compare the observed values of Krassovsky's ratio with values of Krassovsky's ratio from our theoretical model and discuss the implications of the comparison.

6. Instrument Description and Observations

The airglow data presented in this paper were obtained with a Fabry-Perot interferometer (FPI) located at the Arecibo

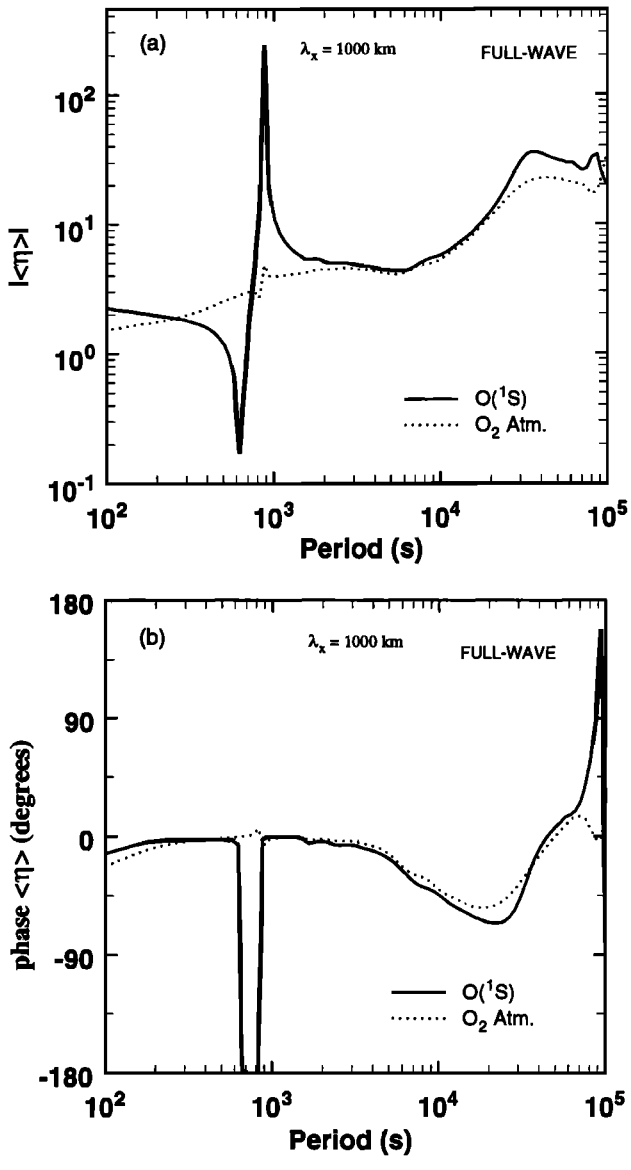

Figure 9. (a) Amplitude and (b) phase of Krassovsky's ratio $\langle\eta\rangle$ versus period for the O(^1S) and O_2 atmospheric airglows. Results are presented for a horizontal wavelength λ_x of 1000 km using the full wave FW theory.

Observatory (18.35° N, 66.75° W). The FPI is a single-etalon, pressure scanned instrument having 15 cm diameter etalon plates. Its field of view was set at 2.25 mrad. Because the measurements were integrated in a column along the viewing direction, we would observe both the E and F region components of the atomic oxygen O(^1S) 557.7 nm airglow. However, during the AIDA campaign we configured the FPI to be more sensitive to the emission from the lower thermosphere by using a 3 cm etalon spacing. This choice of plate separation discriminates against the hotter F region component within the spectral window of the instrument, which then manifests itself as a continuum or constant level in the measurements. Additionally, the O(^1S) emission from the upper thermosphere contributes <20% to the total 557.7 nm emission rate. The result is a sensitivity to the lower thermospheric winds and temperatures without a contamination from the winds and temperatures of the F region. To determine line-of-sight components of the emission, temperature, and neutral wind, as well as the derived horizontal vector components of these parameters and their spatial gradients, we performed a "beam sweep," or map, on the sky, generally in the four cardinal and four 45° off-cardinal azimuth directions at an elevation angle of 30°. We included vertical measurements in each map. For each direction the 557.7 nm emission was scanned twice in wavelength (both increasing and decreasing pressure), usually sampling 12 points across the line with a total integration time of 14 s per spectral point. This yields about 2.8 min between line-of-sight measurements and roughly 25 min resolution for the derivation of the full vector components.

For typical green line emission rates of about 100 R, the integration time is sufficient to collect some 2000 photocounts under the measured line profile, resulting in statistical uncertainties of <10%. However, these errors increase with diminished emission strengths. The wind, temperature, intensity, and background level are determined by a nonlinear least squares fit to the near-Gaussian line shape, a procedure which also determines the uncertainties in the parameters from the reduced chi-square of the fit. The errors were also used as weighting factors in the analysis that determines the vector components.

We applied the analysis of *Burnside et al.* [1981], who determined F region winds and temperature from O(^1D) 630.0 nm observations, to our 557.7 nm spectral measurements. For winds the method assumes that the components of the horizontal neutral wind velocity can be represented by a Taylor expansion about a point directly above the observatory. Only linear terms in the expansion are preserved; that is, we included only the mean flow and the constant horizontal velocity gradients. For temperatures and intensities we both retained the line-of-sight components and also averaged the data in each map to compare with the theory.

For absolute intensity calibration, photometric observations of the 557.7 nm emission intensity were also made in the zenith with a higher time resolution (30 s) than what was used for the Fabry-Perot interferometer. The measured overhead 557.7 nm intensity was determined against a ^{14}C standard source, and this in turn, was used to cross calibrate the signal measured by the FPI. The relative error of the photometric signal is <1% for emission strengths ≥100 R. Further details of the Arecibo instruments, the observational methods, and the analysis techniques used are described by *Burnside et al.* [1981].

Temperature and intensity data as a function of time were detrended by the removal of a best quadratic fit. The detrended data were filtered, interpolated to an evenly spaced grid, smoothed, and windowed. The filtering involved fitting the unequally spaced data with a Fourier series by least squares down to the mean Nyquist frequency. The series was truncated at high frequency to preclude spectral contamination due to large point-to point oscillations in the data. This also serves as an antialiasing measure for the smoothing step. Smoothing was done by a simple three-point averaging. A Hanning data window was then applied to the smoothed data. The smoothed data served as input to the spectral analysis. Both temperature and intensity power spectra were smoothed with a Bartlett spectral window with 6 degrees of freedom (bandwidth of $1.5/(\tau/2)$, where τ is the length of the data set for a given night). The above data analysis procedure removes all waves with periods less than about an hour.

Data that yielded reliable estimates of Krassovsky's ratio are shown in Figure 10. All data shown have been azimuthally

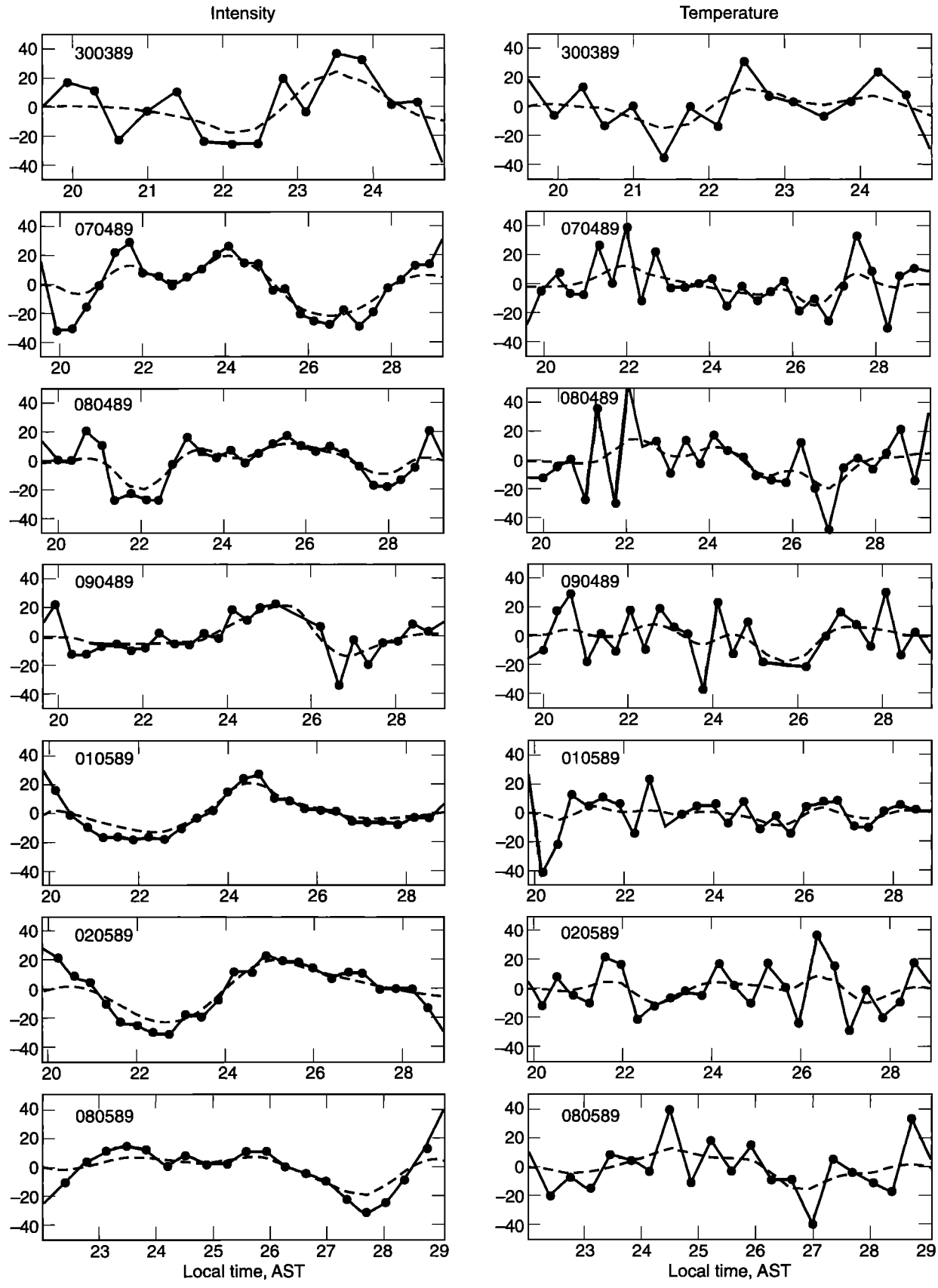

Figure 10. Intensity and temperature fluctuations in observations of the O(^1S) airglow carried out at Arecibo in 1989. The solid lines connect data that were detrended by the removal of a best quadratic fit. The dashed curves show the final results of filtering, interpolating, smoothing, and windowing. Dates in the upper left of each panel are in the format day, month, year.

Table 2. Values of Krassovsky's Ratio $\langle\eta\rangle$ From Observations of O(^1S) Airglow

Case	Period, hours	Amplitude of $\langle\eta\rangle$	Phase of $\langle\eta\rangle$, deg	Coherence
March 30, 1989	5.7	2.2	−42.	0.7
April 7, 1989	10.	3.1	−46.	0.8
April 7, 1989	5.	3.0	−58.	0.6
April 8, 1989	10.1	1.3	−124.	0.8
April 8, 1989	5.	1.5	−117.	0.75
April 9, 1989	9.9	2.1	−154.	0.9
April 9, 1989	4.9	2.2	−144.	0.9
April 9, 1989	3.3	2.0	−127.	0.8
May 1, 1989	9.3	7.0	−155.	0.85
May 1, 1989	4.7	7.6	−150.	0.8
May 2, 1989	9.5	6.5	−6.0	0.6
May 2, 1989	4.7	5.3	11.	0.7
May 8, 1989	7.4	1.4	−3.7	0.75

averaged. The solid lines connect the detrended data, while the dashed curves show the final results of filtering, interpolating, smoothing and windowing described above. Table 2 summarizes the reliable estimates of Krassovsky's ratio inferred from these data. Reliability is based in part on near unity values of the coherence in the cross spectra of the intensity and temperature data [*Hecht et al.*, 1987; *Sivjee et al.*, 1987]. Coherence values for each of the cases in Table 2 are listed.

All the estimates of Krassovsky's ratio in Table 2 are at periods between about 5 and 10 hours (there is one estimate at a period of 3.3 hours). We will see below that $\langle\eta\rangle$ is insensitive to period at these long periods, so it makes sense to average all the estimates of the amplitude of $\langle\eta\rangle$ in Table 2 in order to obtain the most reliable long-period estimate of the magnitude of $\langle\eta\rangle$. The value of $|\langle\eta\rangle|$ at long periods is found to be 3.5 ± 2.2. The large standard deviation reflects the large scatter in the individual estimates of $|\langle\eta\rangle|$. There are basically two groups of $|\langle\eta\rangle|$ values in Table 2, small values of $|\langle\eta\rangle|$ between about 1.5 and 3 and large values of $|\langle\eta\rangle|$ between about 5 and 7. The mean value of $|\langle\eta\rangle|$ and the large standard deviation basically reflect this dichotomy. The groups are not ordered by period.

There are also basically two groups of values for the phase of $\langle\eta\rangle$ in Table 2. One group has values between about 10° and −60°, and the other has values between about −125° and −155°. The two groups of phase values do not comprise the same individual cases as the two groups of $|\langle\eta\rangle|$ values and like the $|\langle\eta\rangle|$ group are not ordered by period. The large negative values of the phase of $\langle\eta\rangle$ suggest that the observed waves are being strongly reflected in the emission layer [*Hines and Tarasick*, 1994].

7. Comparison of Observed and Theoretical Values of Krassovsky's Ratio

The observations of Krassovsky's ratio pertain to long periods between about 5 and 10 hours. Theoretical values of Krassovsky's ratio at periods of 5 and 10 hours are shown in Figure 11 as a function of horizontal wavelength. Since the long-period value of $|\langle\eta\rangle|$ is 3.5 ± 2.2, it is clear from Figure 11a that the observed waves must have horizontal wavelengths of several thousand kilometers. At these long wavelengths, there is little variation of $|\langle\eta\rangle|$ with period in the period range of 5 to 10 hours. At wavelengths of several thousand kilometers and for periods of 5 to 10 hours, Figure 11b shows that the phase of $\langle\eta\rangle$ is between about −50° and −25°. These values are in good agreement with the group of phase observations between about 10° and −60°. However, the group of phase observations between about −125° and −155° must represent waves reflected in the emission layer; reflections not accounted for in the theoretical calculations.

8. Summary and Discussion

From the observations of Krassovsky's ratio and the theory of wave-driven fluctuations in the O(^1S) airglow discussed above, it can be concluded that the gravity waves responsible for the measured airglow variations must have long wavelengths of several thousand kilometers. The near −180° phase of $\langle\eta\rangle$ for a subset of the observations is indicative of wave reflection in the emission layer. Wave reflection can result from altitude variations of temperature or wind velocity, but reflections have not been fully accounted for in the theoretical

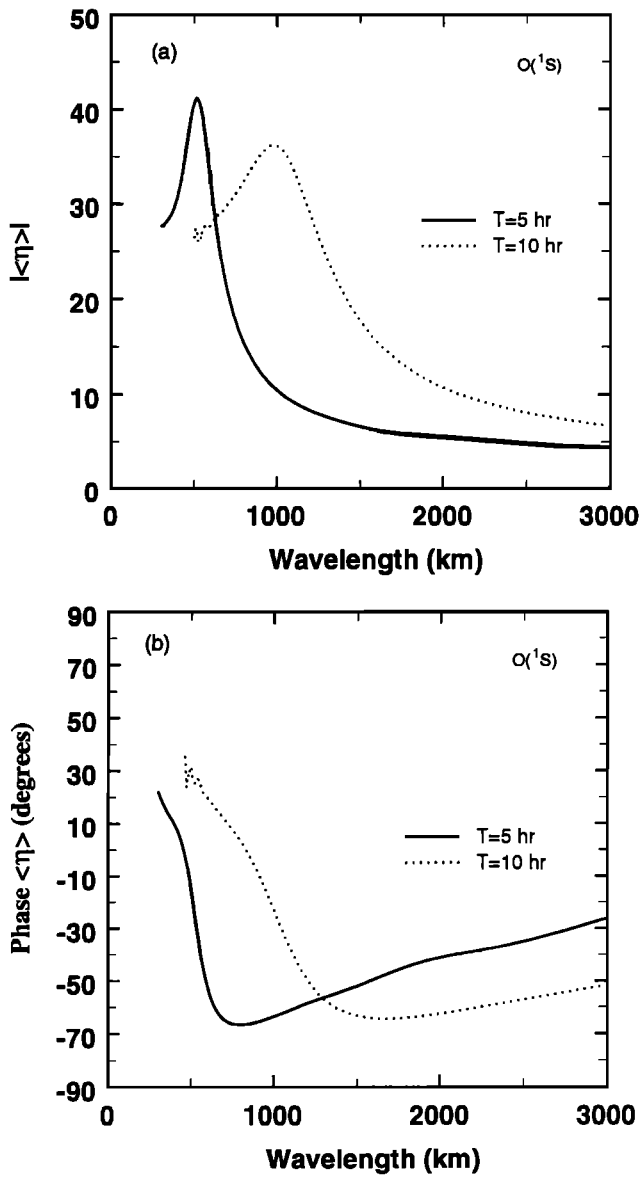

Figure 11. (a) Amplitude and (b) phase of Krassovsky's ratio $\langle\eta\rangle$ versus wavelength at periods of 10 and 5 hours for the O(^1S) airglow on the basis of the full wave theory.

calculations because the observations do not adequately constrain the vertical profiles of winds and temperature. The full wave theoretical model is able to treat gravity wave propagation with arbitrary vertical variations in winds and temperature had we measurements of the full altitude profiles of wind velocity and temperature simultaneous with the airglow observations. *Hickey et al.* [1997, 1998] have already demonstrated the utility of simultaneous O(^1S) airglow and wind velocity measurements in modeling the gravity wave field.

Wind velocities obtained with the data reported here are variable and refer to only the emission layer. Gravity wave modeling requires the full altitude profile of wind velocity. Wind velocities were determined by several techniques [*Hines et al.*, 1993; *Roper et al.*, 1993; *Bird et al.*, 1993] as part of the AIDA'89 campaign, but uncertainties in these velocities are substantial [*Hines et al.*, 1993]. We have investigated the effects of winds on Krassovsky's ratio with idealized altitude profiles of wind velocity including the Cooperative Institute for Research in the Atmosphere (CIRA) zonal mean wind velocity model for April [*CIRA*, 1986]. The CIRA winds compare qualitatively with the measured winds over the several days of observation [e.g., *Roper et al.*, 1993]. The results of these calculations (not shown) indicate that Krassovsky's ratio is essentially unaffected by the winds at the large wavelengths and long periods of interest here. Wind profiles not modeled could have more significant effects on $\langle\eta\rangle$. One observation worth noting, although its implications are not fully understood, is that the largest values of $|\langle\eta\rangle|$ occurred on the only two days in Table 2, May 1, 1989, and May 2, 1989, on which the winds at the level of the emission layer were eastward.

A notable aspect of the data shown in Table 2 is that differences between values of $\langle\eta\rangle$ among various wave periods on a given day are significantly less than the differences among various days for a given wave period. Also characteristic of the data is the preponderance of large negative values of phase ($<-120°$) from April 8, 1989, to May 1, 1989, with several instances of phases $<-150°$. Large negative values of phase can occur as a result of substantial wave reflection [*Hines and Tarasick*, 1994; *Makhlouf et al.*, 1995]. Wave energy is reflected by thermal and Doppler gradients [*Schubert and Walterscheid*, 1984; *Chimonas and Hines*, 1986; *Wang and Tuan*, 1988], and the reflection is especially strong when gradients give contiguous regions of vertical propagation and evanescence. The waves that are most subject to reflection are those with long vertical scales. For the hour-period waves under consideration, waves with long vertical scales have very long horizontal wavelengths (>1000 km); i.e., they have very fast horizontal phase speeds (>200 m s^{-1}). Vertical scales are lengthened by Doppler shifting when a component of the background wind is opposed to the direction of wave propagation. Calculations with standard models of temperature structure indicate that the lower 30 km or so of the thermosphere is a favored region for strong wave reflection. This is a region of high static stability bounded by regions of evanescence for waves with sufficiently long vertical scales. The lower boundary of this region is located near the mesopause. Thus a large reflected component is favored by large horizontal wavelengths, airglow layer centroids above the mesopause, and strong winds opposed to the direction of wave propagation.

The period from April 8, 1989, to May 1, 1989, may have been a period when the O(^1S) airglow layer was largely situated above the mesopause. If so, the dynamical forcing of the airglow fluctuations would have occurred in a region where waves with long horizontal wavelengths might experience strong reflection, especially if they were subject to significant Doppler shifting to higher intrinsic frequencies. We do not know the horizontal wavelengths of the waves in question. However, the data are averaged over all look directions, and this process would effectively eliminate all waves with wavelengths less than about 350 km and would severely attenuate waves at somewhat longer scales. In addition, we do not know the direction of propagation of the waves and do not know how the winds in the airglow layer would project on the wavenumber vector. However, the winds in the region might have been rather strong. The winds for the period when large phases were noted may have approached 100 m s^{-1} during the night [*Roper et al.*, 1993; *Bird et al.*, 1993]. Our wind data give speeds of 20 to 30 m s^{-1} for these times.

We cannot rule out a tidal cause for the wave periods that are not too different from 12 and 6 hours [*Morton et al.*, 1993], especially 12 hours. Insofar as we are aware, values of $\langle\eta\rangle$ for tidally driven 557.7 nm airglow fluctuations are not presently available.

Acknowledgments. Work at The Aerospace Corporation was supported by NASA grants NAGW-2887 and NAG5-4528 and by NSF grant ATM-9714648. Work at Clemson University was supported by NASA grant NAG5-4762 and by NSF grants ATM-9612819 and ATM-9711341. The observations for this study were made at the Arecibo Observatory, which is operated by Cornell University under a cooperative agreement with the National Science Foundation.

Janet G. Luhmann thanks Richard Picard and another referee for their assistance in evaluating this paper.

References

Barth, C. A., The 5577-angstrom airglow, *Science*, *134*, 1426, 1961.

Barth, C. A., Three-body reaction, *Ann. Geophys.*, *20*, 182–196, 1964.

Bates, D. R., The green light of the night sky, *Planet. Space Sci.*, *29*, 1061–1067, 1981.

Bates, D. R., Excitation of 557.7 nm OI line in the nightglow, *Planet. Space Sci.*, *36*, 883–889, 1988.

Bates, D. R., Nightglow emissions from oxygen in the lower thermosphere, *Planet. Space Sci.*, *40*, 211–221, 1992.

Bird, J. C., G. G. Shepherd, and C. A. Tepley, Comparison of lower thermospheric winds measured by a polarizing Michelson interferometer and a Fabry-Perot spectrometer during the AIDA campaign, *J. Atmos. Terr. Phys.*, *55*, 313–324, 1993.

Burnside, R. G., F. A. Herrero, J. W. Meriwether Jr., and J. C. G. Walker, Optical observations of thermospheric dynamics at Arecibo, *J. Geophys. Res.*, *86*, 5532–5540, 1981.

Chapman, S., Some phenomena of the upper atmosphere, *Proc. R. Soc. London, Ser. A*, *132*, 353–374, 1931.

Chimonas, G., and C. O. Hines, Doppler ducting of atmospheric gravity waves, *J. Geophys. Res.*, *91*, 1219–1230, 1986.

Cooperative Institute for Research in the Atmosphere (CIRA), COSPAR international reference atmosphere: 1986, II, Middle atmosphere models, *Adv. Space Res.*, *10*(12), 456–469, 1990.

Gobbi, D., H. Takahashi, B. R. Clemesha, and P. P. Batista, Equatorial atomic oxygen profiles derived from rocket observations of O I 557.7 nm airglow emission, *Planet. Space Sci.*, *40*, 775–781, 1992.

Greer, R. G. H., Oxygen aeronomy and the nightglow: A compact critique, in *Progress in Atmospheric Physics*, edited by R. Rodrigo et al., pp. 97–107, Kluwer, Norwell, Mass., 1988.

Hecht, J. H., R. L. Walterscheid, G. G. Sivjee, A. B. Christensen, and J. B. Pranke, Observations of wave-driven fluctuations of OH nightglow emissions from Sondrestromfjord, Greenland, *J. Geophys. Res.*, *92*, 6091–6099, 1987.

Hedin, A. E., Extension of the MSIS thermosphere model into the middle and lower atmosphere, *J. Geophys. Res.*, *96*, 1159–1172, 1991.

Hickey, M. P., G. Schubert, and R. L. Walterscheid, Seasonal and latitudinal variations of gravity-wave driven fluctuations in OH nightglow, *J. Geophys. Res.*, *97*, 14,911–14,922, 1992.

Hickey, M. P., G. Schubert, and R. L. Walterscheid, Gravity wave-

driven fluctuations in the O_2 atmospheric (0–1) nightglow from an extended, dissipative emission region, *J. Geophys. Res.*, *98*, 13,717–13,730, 1993a.

Hickey, M. P., R. L. Walterscheid, and G. Schubert, A model of wave-driven fuctuations in the O (^1S) nightglow, *EoS Trans. AGU*, *74*(16), Spring Meet. Suppl., 218, 1993b.

Hickey, M. P., R. L. Walterscheid, and G. Schubert, A numerical model of gravity wave propagation in an inhomogeneous atmosphere, *Eos Trans. AGU*, *75*(44), Fall Meet. Suppl., 508, 1994.

Hickey, M. P., R. L. Walterscheid, and G. Schubert, The propagation and dissipation of gravity waves in the terrestrial atmosphere: Full-wave versus WKB models, *Eos Trans. AGU*, 76(46), Fall Meet. Suppl., F436, 1995.

Hickey, M. P., R. L. Walterscheid, G. Schubert, M. J. Taylor, W. Ward, G. G. Shepherd, F. Garcia, M. C. Kelly, and Q. Zhou, Numerical simulations of gravity waves imaged over Arecibo during the 10-day January 1993 campaign, *J. Geophys. Res.*, *102*, 11,475–11,489, 1997.

Hickey, M. P., M. J. Taylor, C. S. Gardner, and C. R. Gibbons, Full-wave modeling of small-scale gravity waves using airborne lidar and observations of the Hawaiian airglow (ALOHA-93) O (^1S) images and coincident NA wind/temperature lidar measurements, *J. Geophys. Res.*, *103*, 6439–6453, 1998.

Hines, C. O., and D. W. Tarasick, Airglow response to vertically standing gravity waves, *Geophys. Res. Lett.*, *21*, 2729–2732, 1994.

Hines, C. O., G. W. Adams, J. W. Brosnahan, F. T. Djuth, M. P. Sulzer, C. A. Tepley, and J. S. Van Baelen, Multi-instrument observations of mesospheric motions over Arecibo: Comparisons and interpretations, *J. Atmos. Terr. Phys.*, *55*, 241–287, 1993.

Kita, K., N. Iwagami, and T. Ogawa, Rocket observations of oxygen night airglows: Excitation mechanisms and oxygen atom concentration, *Planet. Space Sci.*, *40*, 1269–1288, 1992.

Krassovsky, V. I., Infrasonic variations of OH emission in the upper atmosphere, *Ann. Geophys.*, *28*, 739–746, 1972.

Lopez-Gonzalez, M. J., J. J. Lopez-Moreno, and R. Rodrigo, Atomic oxygen concentrations from airglow measurements of atomic and molecular oxygen emissions in the nightglow, *Planet. Space Sci.*, *40*, 929–940, 1992a.

Lopez-Gonzalez, M. J., J. J. Lopez-Moreno, and R. Rodrigo, Altitude profiles of the atmospheric system of O_2 and of the green line emission, *Planet. Space Sci.*, *40*, 783–795, 1992b.

Makhlouf, U. B., R. H. Picard, and J. R. Winick, Photochemical-dynamical modeling of the measured response of airglow to gravity waves, 1, Basic model for OH airglow, *J. Geophys. Res.*, *100*, 11,289–11,311, 1995.

Makhlouf, U. B., R. H. Picard, M. J. Taylor, and J. R. Winick, Gravity waves and vertical diffusion in the lower thermosphere from 557.7 nm airglow, *Adv. Space Res.*, *19*(4), 583–586, 1997.

Makhlouf, U. B., R. H. Picard, J. R. Winick, and T. F. Tuan, A model for the response of the atomic oxygen 557.7 nm and the OH Meinel airglow to atmospheric gravity waves in a realistic atmosphere, *J. Geophys. Res.*, *103*, 6261–6269, 1998.

McDade, I. C., and E. J. Llewellyn, The excitation of O(^1S) and O_2 bands in the nightglow: A brief review and preview, *Can. J. Phys.*, *64*, 1626–1630, 1986.

McDade, I. C., D. P. Murtagh, R. G. H. Greer, P. H. G. Dickinson, G. Witt, E. J. Llewellyn, L. Thomas, and D. B. Jenkinson, ETON 2: Quenching parameters for the proposal precursors of $O_2(b^1\Sigma_g^+)$ and O(^1S) in the terrestrial nightglow, *Planet. Space Sci.*, *34*, 789–800, 1986.

Melo, S. M. L., H. Takahashi, B. R. Clemesha, and J. Stegman, The O_2 Herzberg I bands in the equatorial nightglow, *J. Atmos. Solar Terr. Phys.*, *59*, 295–303, 1997.

Morton, Y. T., J. D. Mathews, and Q. Zhou, Further evidence for a 6-h tide above Arecibo, *J. Atmos. Terr. Phys.*, *55*, 459–465, 1993.

Murtagh, D. P., G. Witt, J. Stegman, I. C. McDade, E. J. Llewellyn, F. Harris, and R. G. H. Greer, An assessment of proposed O(^1S) and $O_2(b^1\Sigma_g^+)$ nightglow excitation parameters, *Planet. Space Sci.*, *38*, 43–53, 1990.

Rees, M. H., *Physics and Chemistry of the Upper Atmosphere*, Cambridge Univ. Press, New York, 1989.

Roper, R. G., G. W. Adams, and J. W. Brosnahan, Tidal winds at mesopause altitudes over Arecibo (18°N, 67°W), 5–11 April 1989 (AIDA'89), *J. Atmos. Terr. Phys.*, *55*, 289–312, 1993.

Schubert, G., and R. L. Walterscheid, Propagation of small-scale acoustic gravity waves in the Venus atmosphere, *J. Atmos. Sci.*, *41*, 1202–1213, 1984.

Schubert, G., and R. L. Walterscheid, Wave-driven fluctuations in OH nightglow from an extended source region, *J. Geophys. Res.*, *93*, 9903–9915, 1988.

Schubert, G., R. L. Walterscheid, and M. P. Hickey, Gravity wave-driven fluctuations in OH nightglow from an extended, dissipative emission region, *J. Geophys. Res.*, *96*, 13,869–13,880, 1991.

Sharp, W. E., The measurement of atomic oxygen in the mesosphere and lower thermosphere, *Planet. Space Sci.*, *39*, 617–626, 1991.

Sivjee, G. G., R. L. Walterscheid, J. H. Hecht, R. M. Hamwey, G. Schubert, and A. B. Christensen, Effects of atmospheric disturbances on polar mesopause airglow OH emissions, *J. Geophys. Res.*, *92*, 7651–7656, 1987.

Slanger, T. G., and G. Black, O(^1S) in the lower thermosphere: Chapman vs. Barth, *Planet. Space Sci.*, *25*, 79–88, 1977.

Strobel, D. F., Constraints on gravity wave induced diffusion in the middle atmosphere, *Pure Appl. Geophys.*, *130*, 533–546, 1989.

Taylor, M. J., and F. J. Garcia, A two-dimensional spectral analysis of short period gravity waves imaged in the OI (557.7 nm) and near infrared OH nightglow emissions over Arecibo, Puerto Rico, *Geophys. Res. Lett.*, *22*, 2473–2476, 1995.

Thomas, L., R. G. H. Greer, and P. H. G. Dickinson, The excitation of the 557.7 nm line and Herzberg bands in the nightglow, *Planet. Space Sci.*, *27*, 925–931, 1979.

Thomas, R. J., Analyses of atomic oxygen, the green line, and Herzberg band in the lower thermosphere, *J. Geophys. Res.*, *86*, 206–210, 1981.

Torr, M. R., D. G. Torr, and R. R. Laher, The O_2 Atmospheric O-O band and related emissions at night from Spacelab 1, *J. Geophys. Res.*, *90*, 8525–8538, 1985.

Walterscheid, R. L., G. Schubert, and J. M. Straus, A dynamical-chemical model of wave-driven fluctuations in the OH nightglow, *J. Geophys. Res.*, *92*, 1241–1254, 1987.

Wang, D. Y., and T. F. Tuan, Brunt-Doppler ducting of small-period gravity waves, *J. Geophys. Res.*, *93*, 9916–9926, 1988.

Witt, G., J. Stegman, B. H. Solheim, and E. J. Llewellyn, A measurement of the ATM atmospheric band and the O I(^1S) green line in the nightglow, *Planet. Space Sci.*, *27*, 341–350, 1979.

G. Schubert and R. L. Walterscheid, Space Sciences Laboratory, The Aerospace Corporation, 2350 East El Segundo Boulevard, El Segundo, CA 90245-4691. (Richard.Walterscheid@notes.aero.org)

M. P. Hickey, Department of Physics and Astronomy, 308 Kinard Laboratory, Clemson University, Clemson, SC 29634-1911. (hickeym@cspar.uah.edu)

C. A. Tepley, Arecibo Observatory, P.O. Box 995, Arecibo, PR 00613-0995. (ctepley@naic.edu)

(Received August 3, 1998; revised February 9, 1999; accepted February 15, 1999.)